Collaborative Research: Efficient Modeling of Incompressible Fluid Dynamics at Moderate Reynolds Numbers by Deconvolution LES Filters - Analysis and Applications to Hemodynamics

Annalisa Quaini[1] and Alessandro Veneziani[2]

[1]Department of Mathematics, University of Houston
[2]Emory University

ANNUAL REPORT – UNIVERSITY OF HOUSTON

July 5, 2020

Research and education activities (Year 1)

Students: 3 graduate students and 2 postdoctoral researchers have been involved in Year 1 of the grant.

- ⋄ Graduate Students:
  - Kayla Bicol (F),
  - Krithika Rathinakumar (F),
  - Giuseppe Pitton (M).
- ⋄ Postdoctoral Researcher:
  - Steffen Basting (M),
  - Yifan Wang (M).

Bicol participated in three conferences and Rathinakumar participated in two conferences. Bicol is the president of the Association of Women in Mathematics Student Chapter at UH. In the Summer 2017 Bicol will participate in the 23rd Industrial Mathematical & Statistical Modeling Workshop for Graduate Students at North Carolina State University. Basting graduated in October 2016 and has been offered a Research Associate position at TU Dortmund (Germany).

Research and education activities (Year 2)

One post-doc (Basting) received a position in Research and Development at Siemens in Germany, while another one (Wang) has accepted a post-doc position at UC Berkeley.

The following **graduate students** continue to work on projects associated with this grant

- Kayla Bicol (F),
- Krithika Rathinakumar (F),
- Daewa Kim (F).

Moreover the following **post-doctoral fellows** have been involved in projects associated with this grant

- Vladimir Yushutin (M),
- Michele Girfoglio (M).

Bicol participated in 2 conferences and Kim participated in 4 conferences. Bicol, Kim, and Rathinakumar are involved in the Association of Women in Mathematics Student Chapter at UH, which will host the Texas Women in Mathematics Symposium in November 2018. Bicol will spend Summer 2018 as an intern at the Naval Research Lab in Monterrey (CA).

Research and education activities (Year 3)

During year 3, the following **graduate students**

- Kayla Bicol (F),
- Krithika Rathinakumar (F),
- Daewa Kim (F).

and the following **post-doctoral fellows**

- Vladimir Yushutin (M),
- Michele Girfoglio (M).

have kept working in projects associated with this grant.

Both Bicol and Kim participated to 5 conferences (TWIMS 2018, SIAM TX-LA Sectional Meeting 2018, JMM 2019, Finite Element Rodeo 2019, AWM Research Symposium 2019). In addition, Bicol participated to SIAM the Geosciences Conference 2019 and Kim attended the 2018 Korean-American Scientists and Engineers Association West Gulf Coast Regional Conference (KSEA-WGCRC). Bicol, Kim, and Rathinakumar are involved in the Association of Women in Mathematics Student Chapter at UH.

Research and education activities (Year 3)

Bicol has accepted a post-doc position with the MIT Mapping Lab, under the mentorship of Dr. Willcox.

Awards: Bicol received the Women and Gender Resource Center's Distinguished Service to Women Award ($1000 Scholarship), University of Houston. Kim received the following awards: AWM award for Graduate Student Conference Travel Grant from the Association for Women in Mathematics, the Best Presentation at the AWM Graduate Student Poster Session at the JMM 2019, and Best Poster at the 2018 KSEA-WGCRC Conference. In addition, Kim was nominate for Best Dissertation within the College of Natural Sciences and Mathematics at the University of Houston.

Research and education activities (Year 4)

During year 3, the following **undergraduate students**

- Kaylee O'Connell (F),
- Quang Hoang (M).

and the following **post-doctoral fellows**

- Martin Hess (M),
- Michele Girfoglio (M).

have kept working in projects associated with this grant.

O'Connell has been supported for the entire Spring semester and has been awarded a Summer Undergraduate Research Fellowship at UH. Hoang's support started at the end of February and is ongoing.

Research and education activities (Year 1)

- **Research Presentations:** Quaini presented the research related to this NSF proposal at over 15 conferences and seminars, which include: Plenary Talk at International Workshop on Fluid-Structure Interaction Problems (Singapore, May 30-June 03 2016), Invited talk at ECCOMAS 2016 (Greece, June 05-10 2016), Seminar at University of Zagreb (Croatia, June 17 2016), Invited talk at 2016 SIAM Conference on the Life Sciences (Boston, July 11-14, 2016), Invited talk at SIMAI 2016 (Italy, September 13-16, 2016), Colloquium Talk at Florida State University (Tallahassee, November 2, 2016), Colloquium Talk at Vanderbilt University (Nashville, January 17, 2017), Invited talk at SIAM CSE 2017 (Atlanta, February 27-March 3, 2017), Invited talk at Workshop on Applied and Computational Mathematics (Houston, March 9, 2017), Plenary Talk at 41st SIAM Southeastern Atlantic Section Conference, Florida State University (Tallahassee, March 18-19, 2017), Invited talk at International Conference on Finite Elements in Flow Problems 2017 (Italy, April 5-7, 2017).

Research and education activities (Year 2)

- **Research Presentations:** during the second year Quaini presented the research related to this NSF proposal at another 8 conferences and seminars: Colloquium Talk at Vanderbilt University (Nashville, April 14, 2017), Invited talk at the 6th international conference on Scientific Computing and Partial Differential Equations (Hong Kong, June 5-8, 2017), Invited talk at the VII International Conference on Coupled Problems in Science and Engineering (Greece, June 12-14, 2017), Invited talk at the AWM workshop within the 2017 SIAM annual meeting (Pittsburgh, July 10-14, 2017), Colloquium Talk at the University of Texas at El Paso (El Paso, September 22, 2017), Colloquium Talk at Rice University (Houston, February 12, 2018), CEE seminar at Duke University (Durham, March 9, 2018), Invited talk at the 42nd SIAM Southeastern Atlantic Section Conference (Chapel Hill, March 9-11, 2018).

Research and education activities (Year 3)

- **Research Presentations:** during the third year Quaini presented
  the research related to this NSF proposal at another 7 conferences
  and seminars: Invited talk at the XIII World Congress on
  Computational Mechanics (New York City, July 22-27, 2018),
  Seminar at the University of Pittsburgh (Pittsburgh, September 25,
  2018), Seminar at the Center for Thermo-Fluid Mechanics,
  University of Houston (Houston, October 30, 2018), Invited talk at
  the 2018 Texas Women in Mathematics Symposium (Houston,
  November 17-18, 2018), Seminar at Brown University (Providence,
  November 30, 2018), Invited talk at the 2019 AWM Research
  Symposium, Rice University (Houston, April 6-7, 2019).

Additional 4 invitations (including a keynote lecture at SCALA 2019,
Tulane University) were declined for medical reasons related to pregnancy
and child birth.

Research and education activities (Year 4)

- **Research Presentations:** during the third year Quaini presented
  the research related to this NSF proposal at another 6 conferences
  and seminars: Invited talk at the VIII International Conference on
  Coupled Problems in Science and Engineering (Spain, June 03-05,
  2019), Invited lecture at the summer school on Reduced Order
  Methods in Computational Fluid Dynamics (Italy, July 08-12, 2019),
  Two invited talks at the 9th International Congress on Industrial and
  Applied Mathematics (Spain, July 5-19, 2019), Invited talk at the
  SIAM conference on analysis of PDEs (La Quinta, December 11-14,
  2019), Keynote talk at Scientific Computing Around Louisiana
  (Baton Rouge, February 07-08, 2020), Invited talk at the ICERM
  workshop on Algorithms for Dimension and Complexity Reduction
  (Providence, March 23-27, 2020).

Several additional talks were canceled due to the COVID-19 pandemic.

Research and education activities (Year 1, 2, and 3)

- **Courses for graduate and undergraduate students:**
  In the spring semesters 2016 and fall semester 2017 Quaini has taught Numerical Analysis for graduate students. In the fall semesters 2016 and 2018 Quaini has taught two sections of Linear Algebra with Matlab, and one section in the spring and fall semester 2017 and spring semester 2018, 2019, and 2020. Topics of this project were mentioned as examples in this course to motivate the students.

- **Organization of Conferences and Workshosp:** Quaini co-organized with Dr. Olshanskii (UH) the Finite Element Rodeo on March 3-4, 2017. The Finite Element Rodeo is an annual, informal conference on finite element methods that rotates between several universities in Texas and Louisiana. Over 70 people participated in the conference, among them many students and post-docs. Quaini is co-chairing with Dr. Rozza (SISSA, Italy) the International Workshop on Reduced Order Methods, to be held at the National University of Singapore in 2021.

Research and education activities (Year 1, 2, and 3)

- **Organization of Special Lectures :** Quaini co-organized with Drs. Gorb and Fitzgibbon (UH) <u>2018 Amundson Lectures</u>, which featured Dr. Bertozzi (UCLA) as the lecturer. The Amundson Lectures were held on April 10-12, 2018 to honor the Prof. Amundson, internationally known for his pioneering work applying mathematical modeling and analysis to the solution of chemical engineering problems. Quaini co-organized with Drs. W. Bangerth (Colorado State), J. Dannberg (UC Davis), T. Heister (University of Utah), and N. Sharma (UTEP) of the <u>Computational Methods for PDEs Summer School</u>, held at Colorado State University, August 3-9, 2019. This summer school was intended to increase diversity in the computational mathematics community.

- **Organization of Mini-Symposia:** Topics from this project have been or will be presented at the following Mini-Symposia organized by Quaini: "LES modeling of turbulence: methods, analysis and applications" at SIAM CSE 2017 (Atlanta, February 27-March 3, 2017), "Fluid-Solid Interaction for Blood Flows" at FEF 2017 (Italy, 04/05-07/17)

Research and education activities (Year 1, 2, and 3)

- **Organization of Mini-Symposia (continued):** "Advanced Models and Methods in CFD" at Coupled Problems 2017 (Greece, 06/12-14/17), "Advances in Reduced Basis techniques for flow problems in analysis, control, and optimization" at the Sixth European Conference on Computational Mechanics (UK, 06/11-15/18), "Advanced Models and Methods in CFD" at 2018 ICOSAHOM (UK, 07/9-13/18), "Reduced Order Methods for Parametric CFD problems" at the 13th WCCM (New York City, 07/22-27/18), "Reduced Order Methods for Parametric CFD problems" at SIAM CSE (Spokane, 02/25-03/01/19), "Advanced models and reduced methods in fluid and fluid-structure interaction problems" at Coupled Problems 2019 (Spain, 06/3-5/19), "Reduced Order Methods for Parametric CFD problems" at ICIAM 2019 (Spain, 07/15-19/2019), "Recent advances in scientific computing and applications" at AMS Fall Central Sectional Meeting 2020 (virtual, 09/12-13/2020).

Main motivation

- Blood flow can be highly disturbed, yet pulsatility prevents turbulence in general.
- In special cases (aortic flow, TCPC, LVAD, etc.) turbulence is observed.
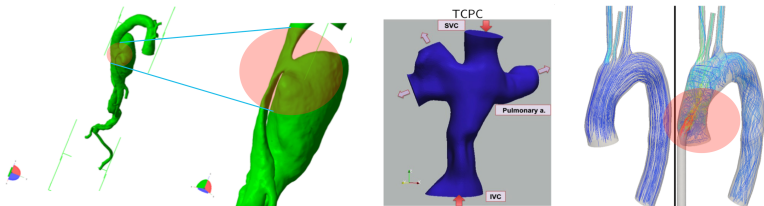
In these cases, Large Eddie Simulation (LES) seems to be a good compromise between Direct Numerical Simulation (DNS, not affordable) and Reynolds-Averaged Navier-Stokes equations (RANS, not accurate).

Limitation of DNS

When $Re \gg 1$, energy is transferred from large eddies to smaller ones up to a characteristic scale, the so called Kolmogorov scale, where they are dissipated by viscous forces.

Kolmogorov scale: $\eta = Re^{-3/4} L$

A direct numerical simulation (DNS) aims at simulating all relevant scales up to the Kolmogorov scale. Therefore, the mesh size has to be $h \approx \eta$.

$$\text{3D simulations:} \quad \#Dofs \sim \left(\frac{L}{h}\right)^3 \sim Re^{9/4}$$

The computational cost required by DNS becomes unaffordable for nowadays computers for Re greater than a few thousands.

Beyond DNS: Our Large Eddy Simulation approach

We choose to use filter stabilization techniques to model and extract the
energy lost to resolved scales due to mesh under-refinement.
The idea is to filter the velocity obtained from the incompressible
Navier-Stokes equations and use as end-of-step velocity a linear
combination of the Navier-Stokes velocity and the filtered velocity.

We interpret these techniques as an **operator-splitting algorithm
(EFR)**: At the time t^{n+1}

1. Evolve: Solve the incompressible Navier-Stokes equations and get
   $\mathbf{v}^{n+1}$, q^{n+1}.

2. Filter: $\mathbf{v}^{n+1} \rightarrow \overline{\mathbf{v}}^{n+1}$, with the associated $\overline{q}^{n+1}$.

3. Relax: $\mathbf{u}^{n+1} = (1-\chi)\mathbf{v}^{n+1} + \chi\overline{\mathbf{v}}^{n+1}$, $p^{n+1} = q^{n+1} + \alpha\chi\overline{q}^{n+1}$.

Step 2 has a key role: to tune the amount and location of eddy viscosity
to the local flow structures.

Step 2: Filter

Given $\mathbf{v}^{n+1}$ from Step 1, find $\overline{\mathbf{v}}^{n+1}$:

$$\rho\frac{\overline{\mathbf{v}}^{n+1}}{\Delta t} - \nabla \cdot \left(2\rho\frac{\delta^2}{\Delta t}a(\mathbf{v}^{n+1})\nabla^s\overline{\mathbf{v}}^{n+1} \right) + \nabla\overline{q}^{n+1} = \rho\frac{\mathbf{v}^{n+1}}{\Delta t},$$

$$\nabla \cdot \overline{\mathbf{v}}^{n+1} = 0,$$

where

- $\delta = O(h)$ is a maximum filtering radius;
- $a(\mathbf{v}^{n+1}) \in (0, 1]$ is the indicator function, with

$$a(\mathbf{v}^{n+1}) \simeq 0 \text{ in regions requiring no local filtering}$$
$$a(\mathbf{v}^{n+1}) \simeq 1 \text{ in regions requiring } O(\delta) \text{ local filtering};$$

- $\overline{q}^{n+1}$ is the Lagrange multiplier for the incompressibility constraint.

The indicator function can be physical phenomenology -based. Such indicator functions are NOT based on rigorous mathematics, thus we preferred to use deconvolution based indicator functions.

Note: this is a Stokes problem! Implementing this approach in a legacy Navier-Stokes solver does not require a big implementation effort.

Validation of our LES approach and novelties

Our LES approach was validated on an benchmark problem proposed by the U.S. Food and Drug Administration within the "Critical Path Initiative".

Goal of the initiative: to advance the application of CFD technology in the development and evaluation of medical devices.

Compare computational results with experimental data[1] for fluid flow in an idealized medical device with rigid boundaries.
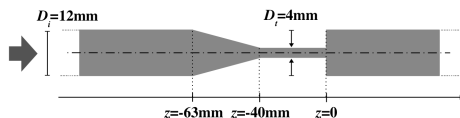
Flow regimes: $Re_t = 2000, 3500, 5000, 6500$.

[Hariharan et al, *J Biomech Engrg* 2011] [Stewart et al, *CVET* 2012] [Stewart et al, *CVET* 2013]

---

[1]https://fdacfd.nci.nih.gov/

LES at $\mathrm{Re}_t = 3500$

We considered several meshes:

mesh name	# nodes	# tetrahedra	Δt
1200k	2.3e5	1.2e6	1e-4
900k	1.8e5	9e5	1e-4
330k	6.5e4	3.3e5	2e-4
140k	3.1e4	1.4e5	3e-4
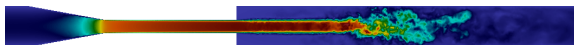
mesh 1200k 240 s on 80 cores
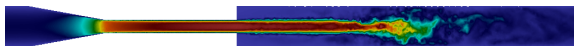
mesh 330k 80 s on 48 cores
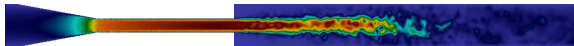
mesh 140k 65 s on 16 cores

The results on mesh 1200k have been obtained with DNS, while the results with meshes 330k and 140k have been obtained with LES. With the coarser meshes, the finer details of the smaller turbulent structures are lost, yet thanks to the our algorithm the average behavior of the flow is well captured.

At $Re = 3500$, the indicator function obtained with mesh $330k$ takes the largest values where the jets breaks down:
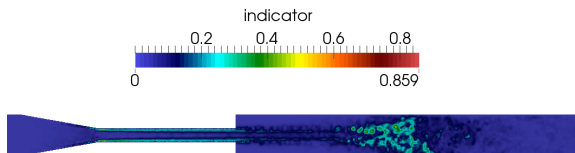
whereas with mesh $140k$ the indicator function takes fairly large values all along the jet:
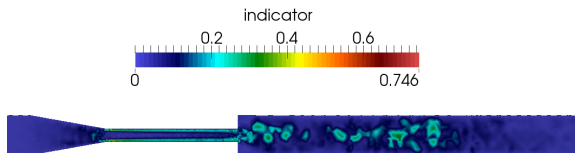
The numerical results obtained with both meshes are in good agreement with the experimental data.

LES at $\text{Re}_t = 5000$

We considered several meshes:

mesh name	# nodes	# tetrahedra	Δt
3000k	5.5e5	3e6	1e-4
1900k	3.7e5	1.9e6	1e-4
900k	1.8e5	9e5	1e-4
330k	6.5e4	3.3e5	2e-4
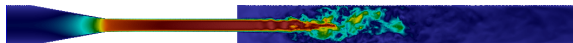
mesh 3000k 280 s on 208 cores
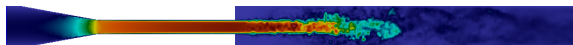
mesh 900k 220 s on 96 cores

Despite the large number of nodes and tetrahedra, mesh 3000k is not refined enough for a DNS to give results in good agreement with the experimental data. We had to use LES with all the meshes and obtained results in good agreement with the experimental data. A paper with all the results obtained with LES has been published in the Int. J. Numer. Meth. Fluids in 2016.

Open-source library

All the computational results presented so far have been performed with LifeV[2], an open-source library of algorithms and data structures for the numerical solution of partial differential equations with high-performance computing techniques. Life V includes solvers for incompressible fluid dynamics, structural problems, and fluid-structure interaction. Life V is written in C++ and is entirely coded with an Object Oriented approach and advanced programming features. Life V was successfully installed on clusters called Maxwell and Opuntia at the UH Center for Advanced Computing & Data System, and on several clusters of the XSEDE consortium.

An important outcome of this work is that the code created for it is incorporated in an open-source library and therefore is readily shared with the community.

---

[2]https://bitbucket.org/lifev-dev/lifev-release/wiki/Home/

EFR algorithm and Finite Volumes

We are interested in understanding the applicability of the EFR algorithm beyond the context of the Finite Element method (FEM), i.e. using a different method to solve the problems at Step 1 and 2. In particular, we consider the Finite Volume method. To solve the Navier-Stokes problem at Step 1, we choose a splitting algorithm called PISO. We use adaptivity in time: the time step in the calculations is governed by the maximum Courant-Friedrichs-Lewy number (CFL_{max}). To solve the Stokes problem at Step 2, we choose another splitting algorithm called SIMPLEC, which features improved convergence. Our approach is validated against numerical data available in the literature for the 2D flow past a cylinder and against the experimental measurements provided by the FDA.

A paper on this work has been published in Computer & Fluids in 2019. The results presented next have been obtained with OpenFOAM[3]. The code created for this work has been incorporated in an open-source library[4].

---

[3] https://www.openfoam.com

[4] https://mathlab.sissa.it/cse-software

2D flow past a cylinder: The quantities of interest are the drag and lift coefficients. In order to understand how refined a mesh should be for a DNS, we perform simulations using several meshes based on prismatic and hexahedral elements. The name of each grid refers to the number of cells and the subscript denotes the kind of element, prismatic (P) or hexahedral (H). We set to $CFL_{max} = 0.2$ and compute the error for the maximum values of the lift and drag coefficients compared to the *true* values from reference [John, *IJNMF* 2004] E_{c_l} and E_{c_d}, respectively.
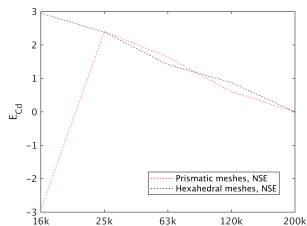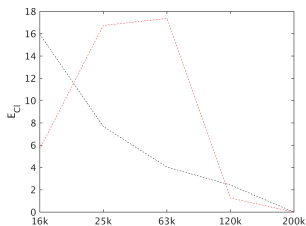
Maximum lift (left) and drag (right) coefficients errors in percentage for the different meshes. We see that for hexahedral meshes the errors decrease monotonically as the mesh is refined, while that is not the case for prismatic meshes. The refinement required by a DNS is 200k cells.

Next, we consider only the hexahedral meshes coarser than mesh $200k_H$ and compare the classical Leray model and our approach for two values of δ: $\delta = h_{min}$ and $\delta = \eta$, where η is the Kolmogorov scale.

Mesh name	Algorithm	E_{c_l}	E_{c_d}
$16k_H$	Leary, $\delta = h_{min}$	-19.59 %	-3.48%
$16k_H$	Ours, $\delta = h_{min}$	7.27%	5.02%
$16k_H$	Leary, $\delta = \eta$	-9.49%	-1.27%
$16k_H$	Ours, $\delta = \eta$	8.68%	4.05%
$25k_H$	Leary, $\delta = h_{min}$	-25.85%	-3.41%
$25k_H$	Ours, $\delta = h_{min}$	2.02%	4.48%
$25k_H$	Leary, $\delta = \eta$	-22.42%	-2.67%
$25k_H$	Ours, $\delta = \eta$	2.02%	4.01%
$63k_H$	Leary, $\delta = h_{min}$	-9.89%	-1.3%
$63k_H$	Ours, $\delta = h_{min}$	2.02%	2.34%
$63k_H$	Leary, $\delta = \eta$	-24.24%	-4.55%
$63k_H$	Ours, $\delta = \eta$	3.03%	5.52 %
$120k_H$	Leary, $\delta = h_{min}$	-6.06%	-0.87%
$120k_H$	Ours, $\delta = h_{min}$	0.8%	1.23%
$120k_H$	Leary, $\delta = \eta$	-26.26%	-5.79%
$120k_H$	Ours, $\delta = \eta$	4.04%	6.96%

In the table on the previous slide, we highlighted in green the simulations that minimize quantity $E_{c_l} + E_{c_d}$. On the hexahedral meshes finer than $25k_H$, our approach with $\delta = h_{min}$ minimizes $E_{c_l} + E_{c_d}$. On mesh $25k_H$, the sum of the errors given by our approach with $\delta = h_{min}$ is slightly larger than the sum of the errors given by our approach with $\delta = \eta$. This is due to the fact that h_{min} of mesh $25k_H$ is comparable to η.

FDA benchmark: The quantities of interest are the normalized axial component of the velocity u_z^{norm} and the normalized pressure difference Δp^{norm}. We compare computed quantities of interest with the experimental data for 4 cases spanning the transitional and turbulent regimes: $Re_t = 2000, 3500, 5000, 6500$. We consider hexahedral meshes with different level of refinement, which is indicated by the mesh name. We made sure that all the meshes feature high quality: low values of maximum non-orthogonality ($20°$ to $25°$), average non-orthogonality (around $4°$), skewness (around 1), and maximum aspect ratio (up to 7). Meshes were selectively refined in the convergent, throat, and sudden expansion.

Normalized axial velocity   Normalized pressure drop
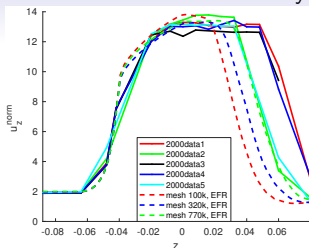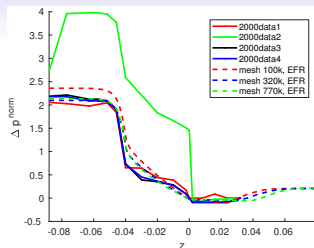
$Re_t = 2000$

$Re_t = 3500$
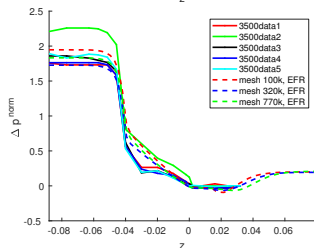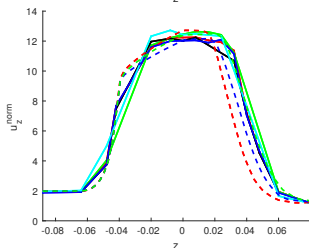
The numerical axial velocity computed with the different meshes are further apart for $Re_t = 2000$ than for all the Reynolds numbers. These results confirm the difficulty in the numerical simulation of the transitional regime. As for the pressure, we observe excellent agreement with the experimental data for both values of Re_t.

Normalized axial velocity   Normalized pressure drop
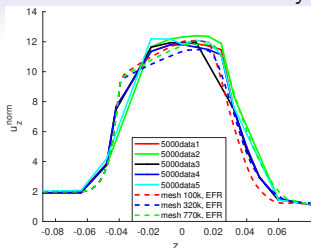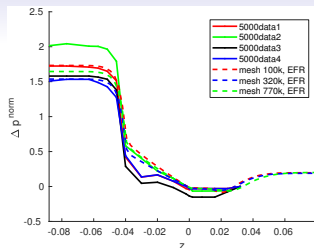
$Re_t = 5000$

$Re_t = 6500$
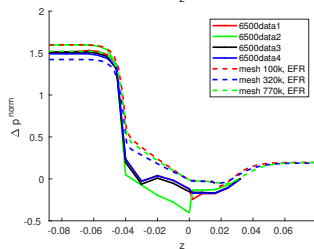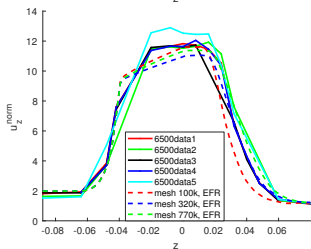
It is remarkable that the results given by the EFR algorithm on a very coarse mesh like $320k$ match so well the experimental data for $Re_t = 5000, 6500$. A possible reason why the results with this mesh were not as good for $Re_t = 3500$ might be that $Re_t = 3500$ is still close to the transitional regime.

From the 2 benchmarks used to assess the EFR algorithm combined with a Finite Volume method, we learned that:

- Hexahedral meshes are to be preferred over prismatic meshes when using the Finite Volume method.
- The computed results are not sensitive to the choice of CFL_{max}.
- The computed results are very sensitive to the choice of scheme for the convective term.
- Also when using the EFR algorithm with the Finite Volume method $\delta = h_{min}$ is the best choice.

Based on our experience, a robust FV-based CFD framework requires:

1. Non-orthogonality and low skewness hexahedral meshes having cells with a contained element aspect ratio.
2. The Central Differencing scheme (2nd order) for the interpolation of the convective term.

Sensitivity to the filtering radius

One critical aspect of filter stabilization techniques for the Large Eddy Simulation of incompressible flows at moderately large Reynolds number (in the range of few thousands) is the selection of the filter radius δ. This drives the effective regularization of the filtering procedure, and its selection is a trade-off between stability (the larger, the better) and accuracy (the smaller, the better). We investigated the sensitivity of the solutions given by our approach to the filter radius by introducing the sensitivity systems, analyzing them at the continuous and discrete levels, and numerically testing on two benchmark problems. We showed that the velocity sensitivity magnitude correctly identifies the region of the domain where the velocity is sensitive to variations of δ. Moreover, we showed that the our approach correctly predicts the physical solution for different values of δ, and is much less sensitive to the parameter choice than the classical Leray model. One paper containing our preliminary work on this has appeared in the Springer-ECCOMAS series "Computational Methods in Applied Sciences" in 2019.

We considered the two dimensional channel flow past a forward-backward step. The correct physical behavior of the solution is a smooth velocity profile, with eddies forming and detaching behind the step. The solutions given by the classical Leray model are similar away from the step, but behind the step they exhibit very different behavior: for $\delta = 0.25$ there is no eddy separation, while for $\delta = 0.1$ the correct transient behavior of eddy shedding is predicted.
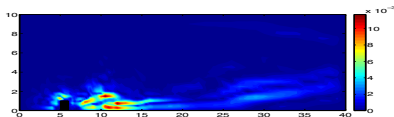

Classical Leray, $\delta = 0.25$ Classical Leray, $\delta = 0.1$
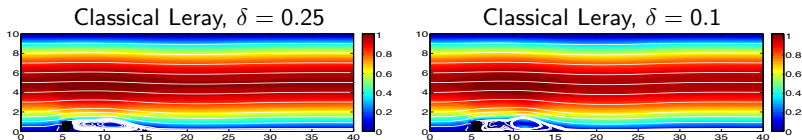
This sensitivity to δ near the step and lack of sensitivity away from the step are predicted in the plot of the velocity sensitivity magnitude for $\delta = 0.25$.
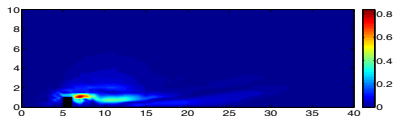
The same test was run with our approach. We observe that both solutions correctly predict eddy shedding behind the step.

Our approach, $\delta = 0.25$ Our approach, $\delta = 0.1$
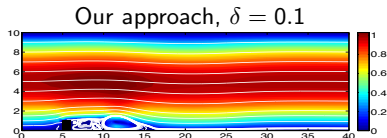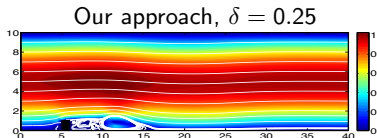
Moreover, we observe that the velocity sensitivity magnitude for $\delta = 0.25$ is quite small. In fact even though it is largest behind the step, just as in the classical Leray case, for our approach the sensitivity magnitude is almost 2 orders of magnitude smaller.

Hence our approach correctly predicts the physical behavior with both choices of δ, and is much less sensitive to the parameter choice than the classical Leray model.

Backflow Stabilization by the EFR algorithm

One of the most problematic aspects in computational hemodynamics is the boundary conditions. Homogeneous Neumann conditions are typically set in the absence of alternatives. This has some drawbacks, particularly for the stability of the physical problem and its numerical consequences. The **flow reversals** occurring in some vascular districts, like the aorta, call for stable solvers.

We observed that with the EFR scheme aortic simulations never suffered from flow reversal instabilities. We discovered that with **the EFR algorithm we may control any backflows** and provided a rigorous proof based on energy considerations and a continuity argument with respect to the parameters, particularly the relaxation parameter χ. While not all the simulations in computational hemodynamics suffer from flow reversal, aorta is one of the districts interested by this phenomenon.

Next, we show the numerical results obtained with a standard Navier-Stokes solver (no LES modeling) and with the EFR algorithm to simulate flow in a patient-specific aorta with an abdominal aneurysm. The patient's aorta is reconstructed from the CT images using VMTK. The data were collected in the frame of the `iCardioCloud` Project. On paper on this work has been published in the Journal of Computational Physics in 2020.

During the deceleration period following the peak systole, the flow is reverted at the brachiocephalic and left subclavian arteries (two supra-aortic vessels, see figure below on the left). The backflow at these two branches causes instabilities and eventually makes a standard Navier-Stokes solver crash. The unstable velocity at the brachiocephalic artery occurring at $t = 0.32$ s is shown below on the right.

Velocity Magnitude (cm/s)
0.000e+00   80   120   160   200   240   280   3.714e+02
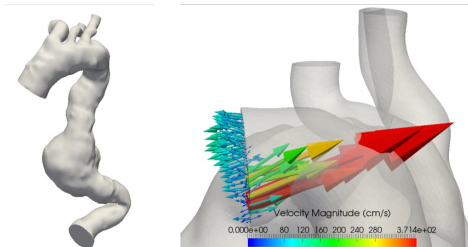
The EFR algorithm successfully suppresses the backflow instability. On the next slide, we compare the results given by the EFR scheme with another common method to treat backflows, i.e. the use of flow extensions that damp the incoming energy carried in by the flow.
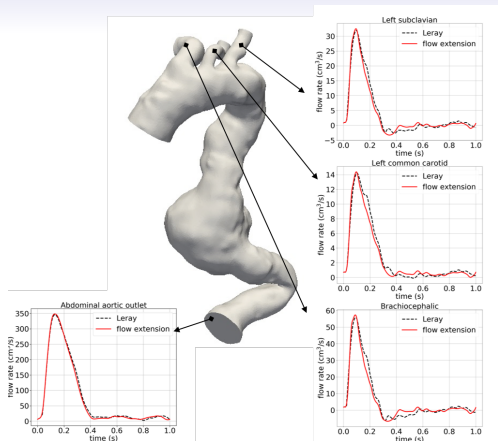
Flow rate computed in the geometry with flow extension and no LES modeling (red line) and in the geometry with no flow extension by the EFR algorithm (dashed black line): comparison at each outflow boundary over time.

The code created for this work is incorporated in LifeV[5].

A filter stabilization technique for advection-diffusion-reaction problems

We adapt to time-dependent advection-diffusion-reaction (ADR) problems the filter stabilization technique proposed in the previous slides for the Navier-Stokes equations. We choose the simplified context of ADR problem to better understand how certain key parameters in the stabilization technique, like filter radius δ and the order of the deconvolution N, affect the solution. It is well known that the Galerkin method for ADR problems can lead to unstable solutions with spurious oscillations when the local Péclet number, which plays a role similar to the Reynolds number, is greater than 1.

The EFR algorithm applied to an ADR problem reads: At the time t^{n+1}

1. Evolve: Solve the ADR equation and get intermediate solution v^{n+1}.
2. Filter: Find $\overline{v}^{n+1}$ such that

$$\overline{v}^{n+1} - \delta^2 \nabla \cdot (a(v^{n+1})\nabla\overline{v}^{n+1}) = v^{n+1}.$$

3. Relax: $u^{n+1} = (1-\chi)v^{n+1} + \chi\overline{v}^{n+1}$.

A deconvolution-based indicator function is given by:

$$a_D(v) = |v - D(F(v))|.$$

A popular choice for D is the Van Cittert deconvolution operator D_N, defined as

$$D_N = \sum_{k=0}^{N} (I - F)^k.$$

The evaluation of a_D with $D = D_N$ requires then to apply the filter F $N + 1$ times.

For $N = 0, 1$, we have:

$$a_{D_0}(\mathbf{v}) = |\mathbf{v} - F(\mathbf{v})|, \quad a_{D_1}(\mathbf{v}) = |\mathbf{v} - 2F(\mathbf{v}) + F(F(\mathbf{v}))|.$$

One manuscript containing our work on this has been appeared in the proceedings of the 2017 FEF Conference. The results presented next have been obtained with FEniCS[6].

---

[6]https://fenicsproject.org

We consider a benchmark test with a prescribed solution given by a hump changing its height in the course of the time. Since the problem is convection-dominated and the solution has a (internal) layer, the use of a stabilization method is necessary. We consider structured meshes with 5 different refinement levels $\ell = 0, \cdots, 4$.
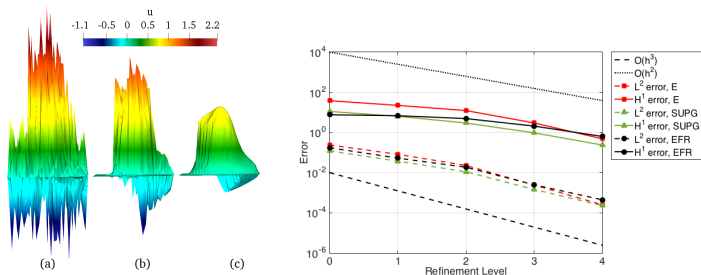
Solution computed on mesh $\ell = 0$ with (a) the standard Galerkin method, (b) the SUPG method, and (c) the EFR method with $\delta = h_{min}$ and $N = 0$. Right: L^2 and H^1 norms of the error for the solution at $t = 0.5$ given by the standard Galerkin method (E), the SUPG method, and the EFR method plotted against the refinement level.

Next, we focus on the EFR algorithm and vary the order of the deconvolution N and the filter radius $\delta = c\, h_{min}$.
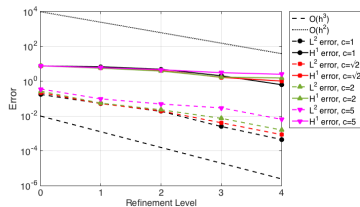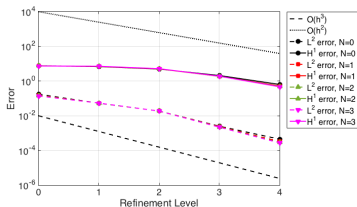
Left: L^2 and H^1 norms of the error for the solution at $t = 0.5$ given by the EFR method with $\delta = h_{min}$ and $N = 0, 1, 2, 3$ plotted against the refinement level. Right: L^2 and H^1 norms of the error for the solution at $t = 0.5$ given by the EFR method with $N = 0$ and $\delta = c\, h_{min}$, $c = 1, \sqrt{2}, 2, 5$, plotted against the refinement level.

The only visible difference when N varies is for the finer meshes, with both errors slightly decreasing as N is increased. The computed solution is much more sensitive to δ than it is to N. These results confirm what we found for the Navier-Stokes equations: $\delta = h_{min}$ is the best choice. It minimizes the error and gives optimal convergence rates. Higher values of c seem to spoil the convergence rate of the EFR method.

LES for Coanda effect in cardiology

Mitral valve Regurgitation (MR) is a valvular heart disease which is associated with the abnormal leaking of blood from the left ventricle (LV) into the left atrium (LA) of the heart. Accurate estimation of regurgitant volume, especially in the case of wall-hugging jets, known as Coanda effect.
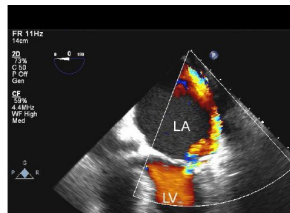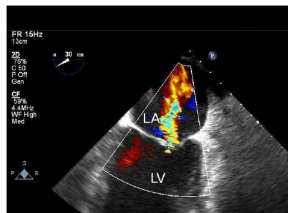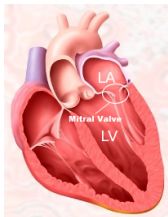
Understanding the flow conditions, and the size of the leaky orifice for which Coanda effect occurs, is one of the biggest challenges of modern echocardiography.

Mock Heart Chamber

A pulsatile flow loop was designed by our collaborators at the Methodist Hospital to model in vitro the hemodynamics conditions encountered in patients with MR. The loop incorporates an anatomically "correct" Mock Heart Imaging Chamber.
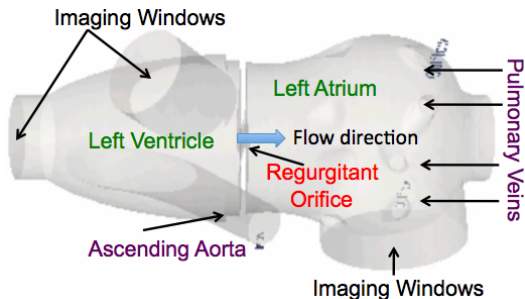
Until now, it was not possible to reproduce Coanda effect *in vitro* in an imaging chamber. The goal is to understand the flow conditions and orifice geometries lead to the Coanda effect *in vitro*.

Simulation of Coanda effect in mock heart chamber

With post-doctoral associate Yifan Wang, we performed 3D simulations of regurgitant flow in the realistic mock heart chamber for a range of Reynolds numbers, including Re = 3000, which corresponds to the realistic regurgitant mitral valve flow. The wall hugging jet (Coanda effect) was observed only at higher Reynolds numbers, and for slender regurgitant orifices. One paper on the simulations of the Coanda effect in mock heart chamber has appeared in Cardiovascular Engineering and Technology in 2017.

3D MOCK HEART CHAMBER

Wall-hugging regurgitant jet
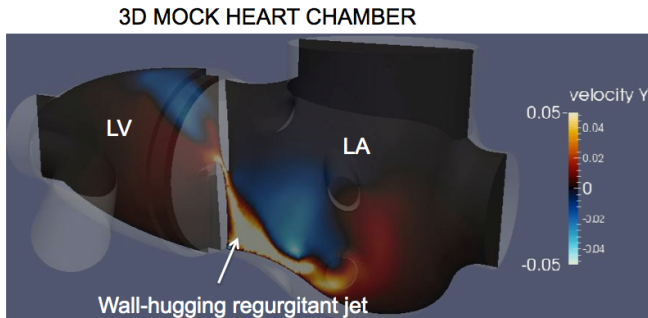
Comparison with 2D color Doppler image

3D simulations of eccentric regurgitant flow were compared with 2D color Doppler image of the same flow in the mock heart chamber. Excellent agreement was achieved. The picture below shows a 2D slice of our 3D simulation (left) and a 2D color Doppler image of the same flow (right). Blue corresponds to backward flow (from top to bottom), while red corresponds to forward flow (bottom to top). A strong wall-hugging regurgitant jet can be observed in both pictures.

3D numerical simulation   2D color Doppler

LA   LA
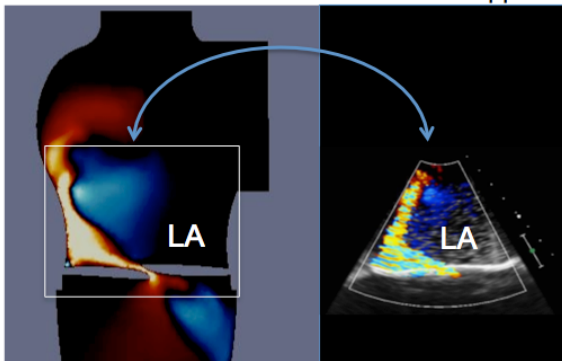
3D Visualization of flow

Our 3D flow simulations for the first time reveal that the regurgitant jet is actually spiraling away from the orifice. A vortex is generated downstream from the orifice, which in 3D generates **vortex rolls**. See Figures on the next page. The vortex rolls push the regurgitant jet even closer to the wall. The spiraling motion of the jet gives rise to the regions of flow that are orthogonal to the imaging source, and would be seen as regions with zero velocity. Due to the low velocity there, as well as on the vortex side, the jet appears smaller than it actually is, giving rise to the under estimation of the regurgitant volume based on the jet appearance on an echocardiographic image.

The figure in the next slide shows the x-component of velocity (left), and the velocity magnitude, together with the velocity vector field (right). The x-component of velocity is toward the viewer. Blue denotes velocity moving away from the viewer, while red denotes velocity moving toward the viewer.

One can see that there is a thin blue region located between the jet and the wall, indicating entrainment of particles associated with Coanda effect. On both sides of the jet there are regions of velocity that are orthogonal to the jet motion, making the jet smaller in appearance on an echocardiographic image.
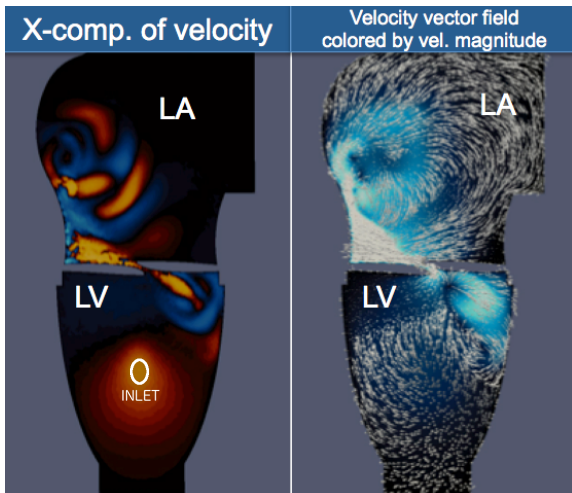
Preliminary results with Reduced Order Modeling

In order to further reduce the computational costs associated with flow simulations, we considered **Reduced Order Modeling** (ROM) techniques. We start by applying standard reduced order methods (e.g., Reduced Basis and/or Proper Orthogonal Decomposition) to the simulation low Reynolds number flow. This is a preliminary step, necessary to understand the capabilities of ROM methods before applying them to high Reynolds number flow. In particular, we focused on the hydrodynamic stability of solutions of the incompressible Navier-Stokes equations for a Newtonian and viscous fluid in 3D. Our preliminary work shows that standard reduced order methods allow to capture complex physical and mathematical phenomena, such as bifurcations in the parametrized Navier-Stokes equations, at a fraction of the computational cost required by full order order methods. One paper reporting on these results has appeared in the Journal of Computational Physics in 2017.

We considered a 3D contraction-expansion channel with fixed aspect ratio $\lambda = 15.4$. We let the normalized channel depth $\mathcal{H}$ (with $\mathcal{H} = 1$ corresponding to the 2D channel) and the Reynolds number vary.
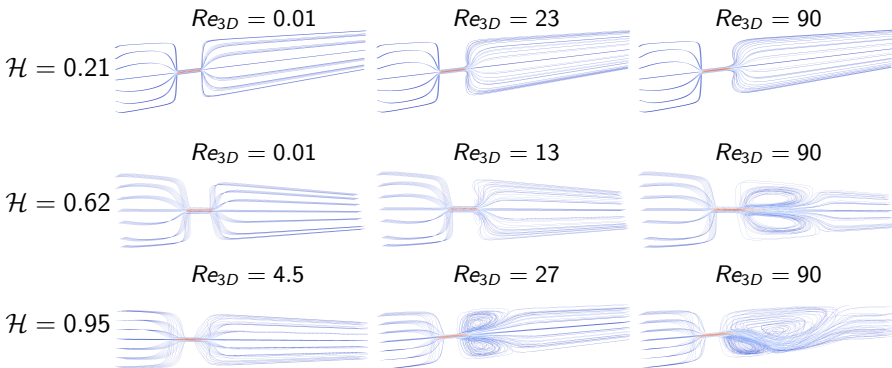
We see that at low values of $\mathcal{H}$ the symmetry breaking bifurcation is pushed to higher values of Re_{3D} due the vertical walls.

The computational time for one simulation with full oder model is 240 CPU hours and with the reduced order model is few seconds.

A localized reduced modeling approach

In order to further reduce the computational cost, we propose a localized ROM approach. In a setting in which the parameter space consists of subregions for which the corresponding solutions of a nonlinear PDE system have different character, such as is the case in the **bifurcation setting**, it may be the case that a standard ROM approach leads to a relatively large, dense system. Thus, it seems prudent to construct several **local bases**, each of which is used for parameters belonging to a different subregion of the bifurcation diagram and also possibly to bridge across the boundary between those subregions.

The key steps in a localized ROM approach are

1. selecting sample points in the parameter domain;
2. computing the corresponding snapshots, i.e., solutions of the full-order discretized problem for each of the parameter points;
3. clustering the snapshots so that each cluster corresponds to parameters in a different part of the parameter domain;
4. constructing the local bases corresponding to each cluster;
5. detecting which cluster a new parameter choice belongs to.

Planar expansion channel

We consider a planar expansion channel with expansion ratio $1:6$. As the Reynolds number increases, the flow configuration is as follows:

Re = 10   Re = 35   Re = 100
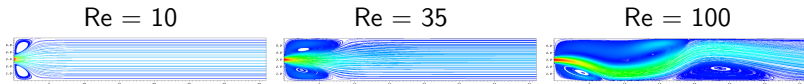
Next, we show the lower stable branch of the bifurcation diagram over Reynolds numbers from 5 to 100 for the Finite Element Method (red) and Spectral Element Method (blue) discretizations, on the left. On the right, we display the k-means variance versus number of clusters for both discretizations.
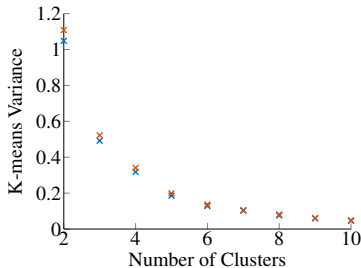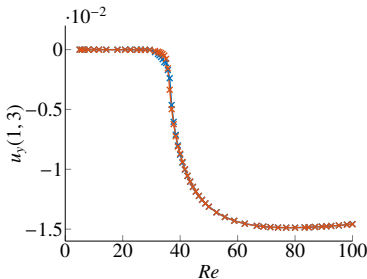
Bifurcation diagram with local ROMs
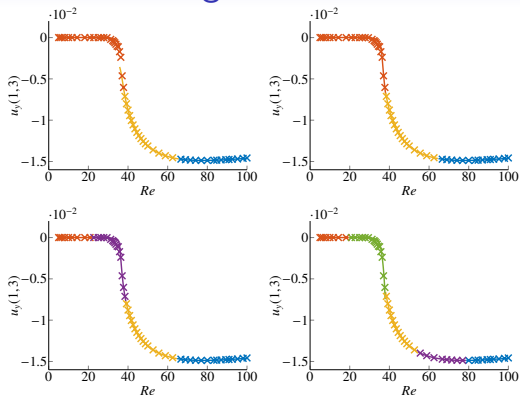
Top: Bifurcation diagrams with 3 local ROMs using the distance to parameter mean criterion (left) and the distance to parameter mid-range and cluster radius criterion (right) to assign the local basis. Bottom: Bifurcation diagrams with 4 (left) and 5 (right) local ROMs using the latter criterion. The 'x' marks full order solutions and color code indicate clustering. The solid lines are ROM solves. Color coding of the solid lines indicate which local ROM was assigned.

The table shows the relative errors at the selected Reynolds numbers of the global ROMs and the 5-cluster local ROMs. The switching between local ROMs occurs at Re = 19.5, Re = 38.1, Re = 54.1 and Re = 78.5 for the cluster midrange/radius criterion. Values marked with (n.c.) correspond to non-converged cases; the iteration loop is terminated after 3000 iterates, whereas convergence typically happens after about 100 iterations.

ROM	Re = 6	Re = 16.333	Re = 26.666	Re = 37	Re = 47.333	Re = 56.666
Global-1	0.00054	0.00052	0.00052	0.0037	0.00079	0.00078
Global-2	0.0043	0.02	0.0082	0.0064	0.0017	0.0019
Local	0.00054	0.00052	0.00060	0.0285	0.015	0.00078

ROM	Re = 68	Re = 78.333	Re = 88.666	Re = 99	mean	max	basis size
Global-1	0.1415 (n.c)	0.240 (n.c)	0.611 (n.c)	0.829 (n.c)	0.18	0.829	54
Global-2	0.0022	0.178 (n.c)	1.64 (n.c)	1.08 (n.c)	0.29	1.64	17
Local	0.0013	0.0084	0.005	0.045	0.011	0.045	10/8/5/14/17

Global-1 and -2 refer to global bases of dimension equal to the sum of the dimensions and to the largest dimension of the local bases, respectively. The tabulated results suggest that the use of local reduced bases provide a more accurate ROM approach when compared to the use of global reduced bases.

Two parameter study

We consider jet flow with variable kinematic viscosity ν and emanating from an orifice of variable width w, symmetrically located with respect to the channel centerline.
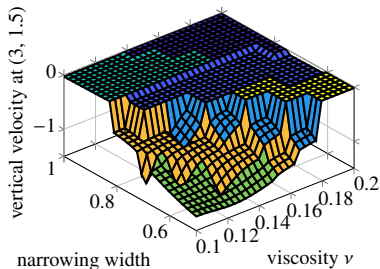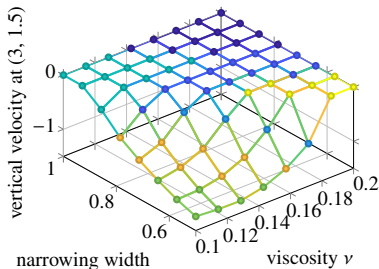
Left: steady state vertical component of the velocity computed by Spectral Element Method and evaluated at the point $(3.0, 1.5)$. A different marker color is used for each of the 7 clusters. Right: bifurcation diagram and assignment of parameters to local ROMs using the closest snapshot location criterion.

One paper on our localized ROM approach has appeared in Comput. Methods Appl. Mech. Engrg. in 2019.

ROM for Navier-Stokes equations with linear filtering stabilization

We propose a Proper Orthogonal Decomposition (POD)-Galerkin based Reduced Order Model (ROM) for a Leray model with a linear differential low-pass filter. For the implementation of the model, we combine the Evolve-Filter algorithm (EFR with no relaxation) with a computationally efficient Finite Volume method. The main novelty of the proposed approach relies in applying spatial filtering both for the collection of the snapshots and in the reduced order model. In both steps of the EF algorithm, velocity and pressure fields are approximated by using different POD basis and coefficients. For the reconstruction of the pressures fields, we use a pressure Poisson equation approach. This work is a first step towards the development of a ROM for a Leray model with a nonlinear differential filter, which we have shown to be accurate for high Reynolds number flow (up to 6000). One manuscript reporting on these results is in preparation.

2D flow past a cylinder

We computed the evolution of the solution with a Full Order Model (FOM) and our ROM.
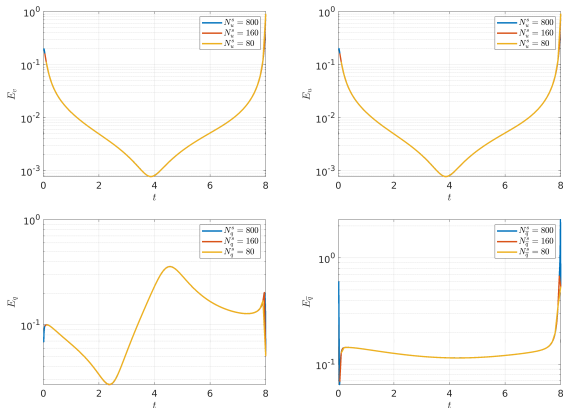
Time history of L^2 norm of the relative error for the velocity fields (top) and pressure fields (bottom) for different numbers of snapshots, i.e. different sampling frequencies. Evolve (resp., Filter) step on the left (resp., right).

The FOM/ROM comparison for the drag and lift coefficients over time is reported below.
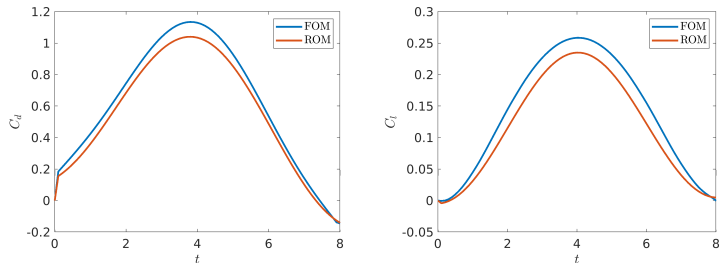
We observe that the amplitude of the force coefficients are slightly underestimated for all the time instants by our ROM approach. The ROM reconstruction of the lift coefficient appears to be more critical, especially around the center of the time interval. This could be due to the fact that larger errors for the Evolve pressure are localized close to the cylinder.

3D flow past a cylinder

The difference between FOM and ROM Filer velocity (left) and Filter pressure (right) at time $t = 5$ is shown below.
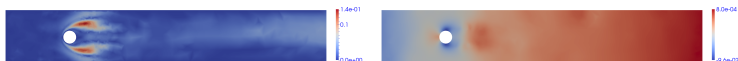
As for the aerodynamics coefficients, the relative errors related for the maximum values are $E_{c_d} = 0.3\%$ and $E_{c_l} = 17.9\%$. A better reconstruction of the maximum C_l is obtained by using a higher number of modes for the pressure in order to reconstruct more accurately the low amplitude oscillatory pattern around the time the peak is reached. When switching from 4 to 15 modes, the C_l error decreases from 17.9% to 3.6%.

We found that our ROM approach is able to reproduce the main flow features for problems in 2D and 3D. In addition, the accuracy of our approach is comparable to to other ROMs presented in the literature and applied to time dependent flow problem.

Fluid-structure interaction with a DG-ALE approach

In many cardiovascular applications, blood (modeled as an incompressible, viscous, and Newtonian fluid) interacts with an elastic/viscoelastic structure such as cardiovascular tissue or vascular prosthesis. We proposed a numerical approach based on a high-order discontinuous Galerkin (with Interior Penalty) method, combined with the Arbitrary Lagrangian-Eulerian approach to deal with the motion of the fluid domain, which is not known a priori. The proposed numerical approach provides sharp resolution of jump discontinuities in the pressure and normal stress across fluid-structure and structure-structure interfaces.

The proposed numerical method has been tested on a series of benchmark problems, and has been applied to a fluid-structure interaction problem describing the flow of blood in a patient-specific aortic abdominal aneurysm (AAA) before and after the insertion of a prosthesis known as stent-graft. The stent-graft excludes the aneurysm sack from circulation and lowers the probability of AAA rupture. One paper on this work has appeared in the Journal of Scientific Computing in 2018.
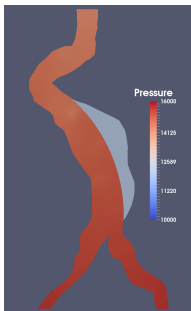
AAA before and after stent-graft

The figures below show the computed pressure p without and with stent-graft (SG) and the computed velocity magnitude $||\mathbf{u}||$ and vector field without and with stent-graft at roughly $1/3$ of the cardiac cycle:
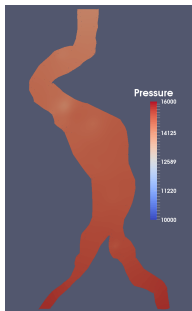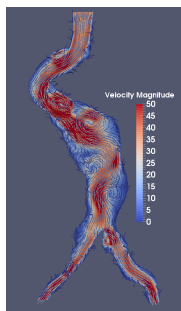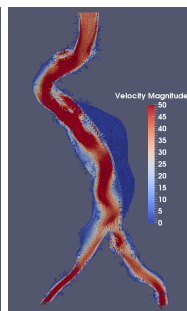
   p without SG p with SG $||\mathbf{u}||$ without SG $||\mathbf{u}||$ with SG

The proposed DG method provides a sharp resolution of the pressure jump that occurs across the stent graft. We see that after the stent graft implantation the vortices are inhibited and confined, and the pressure exerted onto the aneurysm sack walls is reduced.

A finite element method for Stokes equation on surfaces

We consider a Stokes problem posed on a 2D surface Γ embedded in a 3D domain:

$$-2\nu\mathbf{P}\mathrm{div}_\Gamma(\mathbf{D}_\Gamma(\mathbf{u})) + \nabla_\Gamma p = \mathbf{f} \quad \text{on } \Gamma, \quad \mathbf{D}_\Gamma(\mathbf{u}) = \left(\nabla_\Gamma\mathbf{u} + \nabla_\Gamma^T\mathbf{u}\right)/2$$

$$\mathrm{div}_\Gamma\mathbf{u} = g \quad \text{on } \Gamma, \quad \mathbf{u}\cdot\mathbf{n} = 0 \quad \text{on } \Gamma$$

The equations serve as a model problem in the dynamics of material interfaces.

We want to use an unfitted Finite Element method called TraceFEM, which features accuracy $\geq O(h^2)$.

The idea behind TraceFEM is to use a trace space induced by FE functions for the bulk triangulation $\mathcal{T}_h$.

2D illustration

Γ

$\mathcal{T}_h$
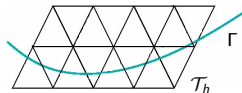
TraceFEM for Stokes equation on surfaces

Ingredients of our approach:

- Finite elements induced by $\mathbb{P}_1$ bulk finite elements for both the velocity and the pressure.
- A penalty term in order to enforce the velocity vector field to be tangential to the surface.
- A stabilization term that resembles the Brezzi-Pitkäranta stabilization for the planar Stoles $\mathbb{P}_1 - \mathbb{P}_1$ finite element pair.
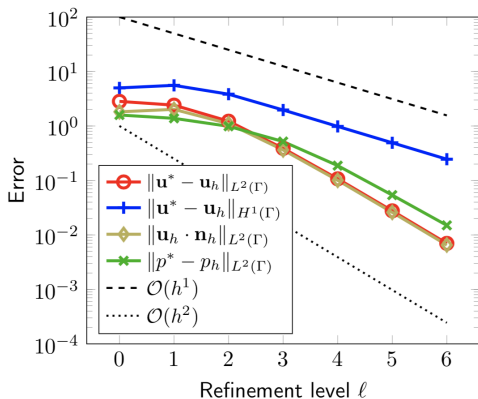- A normal stabilization term to avoid issues in case of small element cuts.

We prove:

- ⋄ Stability.
- ⋄ Optimal order discretization error bounds in the surface H^1 and L^2 norms.

Space convergence

The surface Γ is the unit sphere, centered at the origin. We consider the following exact solution
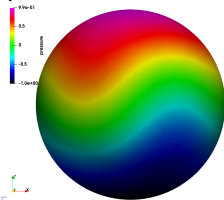
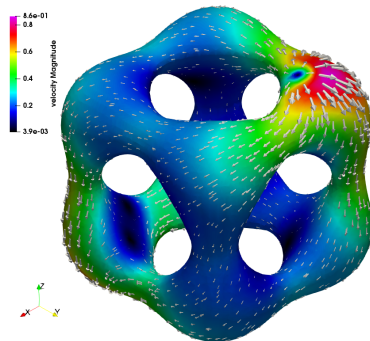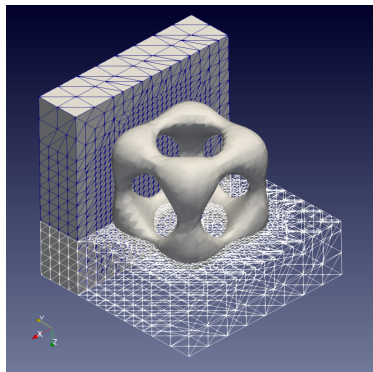$$\mathbf{u}^* = \mathbf{P}(-z^2, y, x)^T, \quad p^* = xy^3 + z,$$

velocity
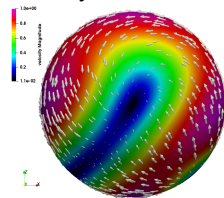
pressure

Flow on a complex manifold

We consider the unsteady surface Stokes problem posed on a more complex manifold. The flow is driven by the non-zero source term in the mass balance equation.

On paper on this work has been published in the SIAM Journal on Scientific Computing in 2018.

Lateral phase separation with phase transition

We consider phase separation on smooth closed surface $\Gamma \subset \mathbb{R}^3$. Let η be an order parameter and c be a representative concentration.

Non-conservative model: surface Allen–Cahn equation

$$\frac{\partial \eta}{\partial t} + \alpha f_0'(\eta) - \alpha \epsilon^2 \Delta_\Gamma \eta = 0 \quad \text{on } \Gamma$$

Conservative model: surface Cahn–Hilliard equation

$$\rho \frac{\partial c}{\partial t} - \text{div}_\Gamma \left(M \nabla_\Gamma \left(f_0'(c) - \epsilon^2 \Delta_\Gamma c \right) \right) = 0 \quad \text{on } \Gamma$$

$\alpha > 0$: a kinetic coefficient ϵ: gradient energy coefficient

$f_0(u) = \frac{1}{4}(u-1)^2 u^2$: specific free energy (Ginzburg-Landau potential)

$M = M(c) = c(1-c)$: mobility coefficient (degenerate)

In order to have phase separation, f_0 must be a non-convex function of its argument

On paper on this work has been published in the Int. J. Numer. Meth. Biomed. Eng. in 2019.
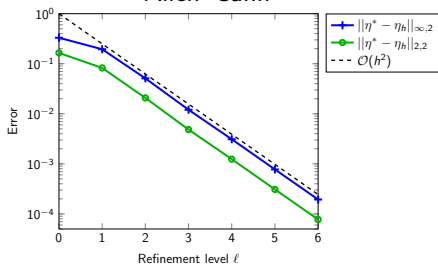
Convergence test

We apply TraceFEM ($\mathbb{P}_1$ bulk finite elements) to the surface Allen–Cahn and Cahn–Hilliard equations. We consider the following exact solutions
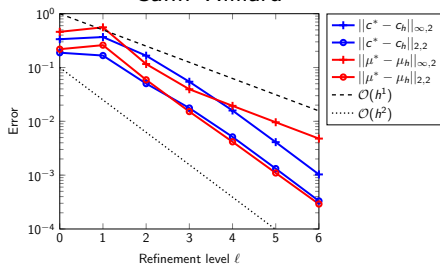
$$\eta^* = c^* = \frac{1}{2}\left(1 - 0.8e^{-0.4t}\right)\left(Y(x_1, x_2) + 1\right), \quad Y(x_1, x_2) = x_1 x_2, \quad t \in [0, 5]$$

with $\epsilon = 0.1$, $\Omega = [-5/3, 5/3]^3$, Γ is unit sphere, $h_\ell = \frac{10/3}{2^{\ell+1}}$, $\Delta t = 2^{-(1+\ell)}$.
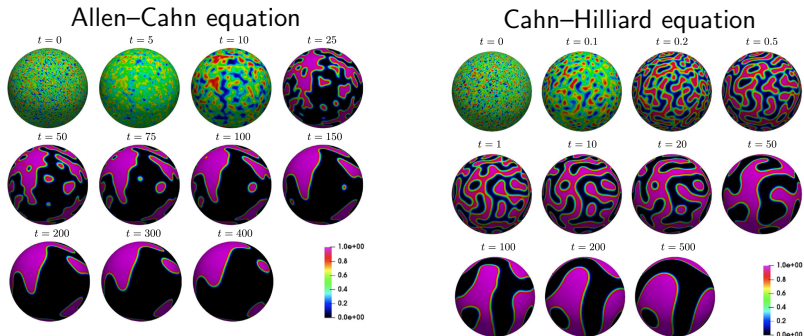

Allen–Cahn

Cahn–Hilliard

We observe optimal order of convergence in the discrete $L_\infty(0, T; L^2(\Gamma_h))$ norm and discrete $L_2(0, T; L^2(\Gamma_h))$ norm for both problems.

Sphere

Lateral phase separation of a two-component mixture with random initial condition, stopped close to steady state, $\epsilon = 0.01$

We see that after the initial fast stage, which ends in a little more than ten time units (resp., one tenth of time unit) for the Allen–Cahn (resp., Cahn–Hilliard) equation, there is a considerable slow down in the evolution of the solution. After that, we notice a further deceleration in the process of dissipation of the interfacial energy.
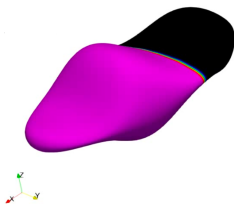
Idealized cell

We consider the surface given implicitly by: $\Gamma = \mathbf{x} \in \mathbb{R}^3$, $\phi(\mathbf{x}) = 0$, with

$$\phi(\mathbf{x}) = \frac{1}{4}x_1^2 + x_2^2 + \frac{4x_3^2}{(1 + \frac{1}{2}\sin(\pi x_1))^2} - 1.$$
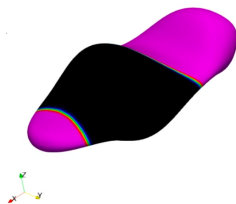
Unlike the sphere, on this surface it is possible to trace a curve of minimal length.

Lateral phase separation close to steady state:

Allen–Cahn model   Cahn–Hilliard model

- Limiting behavior ($\epsilon \to 0$) of the Allen–Cahn equation is mean curvature motion, which generalizes to geodesic curvature motion for surfaces. [Evans et al., *Commun. Pure Appl. Math* 1992]
- Limiting behavior ($\epsilon \to 0$, $t \to \infty$) of the Cahn–Hilliard equation is a minimal perimeter problem. [Modica, *ARMA* 1987]

Lateral phase separation on an evolving surface

Using elementary tangential calculus, we derive a Cahn–Hilliard problem posed on an evolving material surface:

$$\dot{\rho} + \rho \operatorname{div}_\Gamma \mathbf{u} = 0 \quad \text{on } \Gamma(t)$$

$$\dot{c} - \rho^{-1} \operatorname{div}_\Gamma \left(M \nabla_\Gamma \left(\frac{1}{\epsilon} f_0' - \epsilon \Delta_\Gamma c \right) \right) = 0 \quad \text{on } \Gamma(t)$$

where $\dot{f}$ is the material derivative of f.

- Total conservation of mass
- Conservation of mass for one component

[Elliott-Ranner, *Numer. Math.* 2015]

Lateral phase separation on an evolving surface

Using elementary tangential calculus, we derive a Cahn–Hilliard problem posed on an evolving material surface:

$$\dot{\rho} + \rho \mathrm{div}_\Gamma \mathbf{u} = 0 \quad \text{on } \Gamma(t)$$

$$\dot{c} - \rho^{-1} \mathrm{div}_\Gamma \left(M \nabla_\Gamma \left(\frac{1}{\epsilon} f_0' - \epsilon \Delta_\Gamma c \right) \right) = 0 \quad \text{on } \Gamma(t)$$

where $\dot{f}$ is the material derivative of f.

- Total conservation of mass
- Conservation of mass for one component

[Elliott-Ranner, *Numer. Math.* 2015]

Lateral phase separation on an evolving surface

Using elementary tangential calculus, we derive a Cahn–Hilliard problem posed on an evolving material surface:

$$\dot{\rho} + \rho \operatorname{div}_\Gamma \mathbf{u} = 0 \quad \text{on } \Gamma(t)$$

$$\dot{c} - \rho^{-1} \operatorname{div}_\Gamma \left(M \nabla_\Gamma \left(\frac{1}{\epsilon} f_0' - \epsilon \Delta_\Gamma c \right) \right) = 0 \quad \text{on } \Gamma(t)$$

where $\dot{f}$ is the material derivative of f.

- The system is one-way coupled
- We are not aware of a minimization property for the Cahn–Hilliard problem in time-dependent domains $\rightarrow$ the system is no longer dissipative

[Elliott-Ranner, *Numer. Math.* 2015]

Evolving surface case: weak formulation

To be able to use an Eulerian approach, we introduce an arbitrary smooth extension of c and μ to a neighborhood

$$\mathcal{O}_\delta(\Gamma(t)) = \{\mathbf{x} \in \mathbb{R}^3 \, : \, \text{dist}(\mathbf{x}, \Gamma(t)) < \delta\}.$$

and reformulate the problem in terms of the extended variables.

The weak formulation becomes:

$$\int_{\Gamma(t)} \rho \left(\frac{\partial c}{\partial t} + \mathbf{u} \cdot \nabla c \right) v \, ds + \int_{\Gamma(t)} M \nabla_\Gamma \mu \, \nabla_\Gamma v \, ds = 0,$$

$$\int_{\Gamma(t)} \mu \, q \, ds - \frac{1}{\epsilon} \int_{\Gamma(t)} f_0'(c) \, q \, ds - \epsilon \int_{\Gamma(t)} \nabla_\Gamma c \, \nabla_\Gamma q \, ds = 0,$$

$$\frac{\partial \mu}{\partial \mathbf{n}} = \frac{\partial c}{\partial \mathbf{n}} = 0 \quad \text{in } \mathcal{O}_\delta(\Gamma(t)),$$

for all smooth v and q defined in $\Gamma(t)$.

Evolving surface case: discretization

We assume that

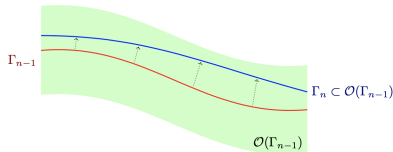$$\Gamma^n \subset \mathcal{O}_\delta(\Gamma^{n-1})$$

for $n = 1, \ldots, N$.

Then, c^{n-1} is defined on Γ^n and we can write

$$\frac{\partial c}{\partial t} \approx \frac{c^n - c^{n-1}}{\Delta t} \quad \text{on } \Gamma^n$$

We discretize first in time (semi-implicit Euler method) and then apply TraceFEM for space discretization.

Everything else is like the stationary surface case.

Oscillating ellipsoid

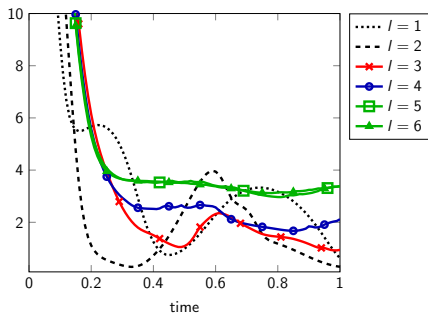We consider time-dependent surface $\Gamma(t)$ to be an oscillating ellipsoid. As initial solution, we take:

$$c_0 = 0.5 + 0.05\cos(2\pi x_1)\cos(2\pi x_2)\cos(2\pi x_3).$$

We set $\epsilon = 0.01$, $h_\ell = \frac{10/3}{2^{\ell+2}}$, $\Delta t = 0.01$.

Discrete Lyapunov energy:

$$E_h^L(c_h) = \int_{\Gamma_h} f(c_h)\,ds$$

[Elliott-Ranner, *Numer. Math.* 2015]

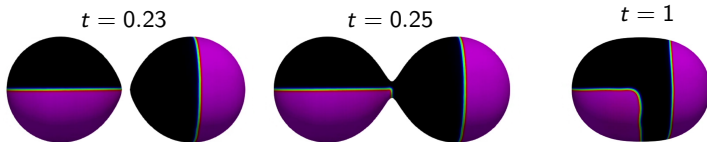# Colliding spheres with pre-separated phases

The evolving surface is the zero level set of level set function

$$\phi(\mathbf{x}, t) = 1 - \frac{1}{||\mathbf{x} - \mathbf{x}_c^+(t)||^3} - \frac{1}{||\mathbf{x} - \mathbf{x}_c^-(t)||^3},$$

with

$$\mathbf{x}_c^{\pm}(t) = \pm \left(\frac{3}{2} - t, 0, 0 \right), \quad t \in [0, 1.5].$$

We take an initial solution with pre-separated phases on each ball.

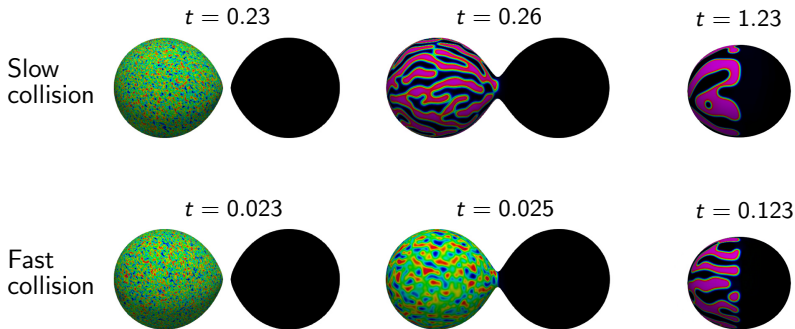$t = 0.23$ $t = 0.25$ $t = 1$

Pattern formation on colliding spheres

Same surface dynamics as before, but different initial condition:

- two-component mixture with random initial condition (1:1) for the ball initially centered at $\mathbf{x}_c^-(0)$
- homogeneous phase for the ball initially centered at $\mathbf{x}_c^+(0)$

We set $\epsilon = 0.01$.

One paper reporting on these results has appeared in the Journal of Computational Physics in 2020 and another one has been submitted.

Plans for the Next Reporting Period

- Extend the ROM approach to the EFR algorithm.
- Improve the criterion to assign the local ROM basis in multi-parameter studies using a Machine Learning approach.